American Mineralogist, Volume 91, pages 1807–1814, 2006

Finite element modeling of elastic volume changes in fluid inclusions: Comparison with experiment

PAMELA C. BURNLEY[1,*] AND CHRISTIAN SCHMIDT[2]

[1]Department of Geosciences, Georgia State University, P.O. Box 4105, Atlanta, Georgia 30302-4105, U.S.A.
[2]GeoForschungsZentrum Potsdam, Telegrafenberg, 14473 Potsdam, Germany

ABSTRACT

We have used finite element modeling (FEM) to successfully reproduce elastic volume changes of synthetic fluid inclusions in quartz pressurized in a hydrothermal diamond-anvil cell (HDAC) at external pressures up to 250 MPa. At higher pressures, the synthetic inclusions are somewhat stiffer than would be predicted by linear elasticity due to the effect of pressure on the elastic moduli. The finite element models were created to reproduce the inclusion's approximate shape, and crystallographic orientation within the host, which is elastically anisotropic. The models successfully predict changes in fluid inclusion volume measured using the HDAC, which gives us confidence that FEM may be used to predict the elastic behavior of inclusions in other situations.

Keywords: Mechanical properties, elastic volume change, high-pressure studies, hydrothermal diamond anvil cell, metamorphic petrology, fluid inclusion, finite element modeling, elastic deformation, volume change

INTRODUCTION

Inclusions within mineral grains are nearly ubiquitous in rocks of all types. Whether they are crystalline, glass, fluid, or gas, inclusions contain information about either the environment of formation of the host mineral grain or in the case of secondary fluid inclusions, conditions since the mineral grain was formed. If the temperature or pressure changes after the inclusion-host system forms, differences in thermal expansion or compressibility between the two will create differential stresses in the host and may cause it to permanently deform. In many situations, understanding the mechanics of the inclusion-host system is helpful for interpreting measurements made on the inclusion. For example, interpretation of homogenization temperatures of fluid inclusions is based on the assumption that the inclusion's volume has not changed since trapping (Roedder 1984). For solid inclusions, patterns of cracks in the host or measurement of the internal pressure within the inclusion may be useful in deducing information about the geologic history of a sample (e.g., Kenkmann and Dresen 1998; Whitney et al. 2000). Fluid and melt inclusions can be studied using a hydrothermal diamond-anvil cell (HDAC) to prevent decrepitation and/or water loss. In such studies, elastic changes of the inclusion volume due to the application of high confining pressures can lead to significant changes in the measured phase transition temperature (Darling and Bassett 2002; Schmidt et al. 1998). The elastic volume change as a function of pressure depends on the inclusion geometry (Burnley and Davis 2004). Therefore, it must be determined for individual inclusions, either empirically or by modeling, to correct measured phase transition temperatures for the stress-related component of the volume change. In an effort to test the utility of finite element models for understanding the mechanical behavior of inclusions in minerals, we have compared measured elastic volume changes and deformation of synthetic pure water inclusions in quartz with finite element models of the individual inclusions. Such inclusions are ideal for this study. The internal pressure, as well as associated elastic and plastic volume changes of the inclusion can be determined accurately from the homogenization temperature because reliable data are available for the molar volume along the liquid-vapor curve of water. Therefore, all the mechanical boundary conditions as well as the resulting deformation are known and can be compared to those produced under the same conditions in the model. Finite element models are useful because they can be used to reproduce more complex shapes than can be modeled analytically and the elastic anisotropy of the host can be included.

METHOD

Hydrothermal diamond-anvil cell experiment

The experimental set-up for this study is shown schematically in Figure 1. We used an externally heated hydrothermal diamond-anvil cell (HDAC) (Bassett et al. 1993). The thermal gradients within the sample chamber are small, which permits accurate and reproducible temperature measurements. Slow heating rates and stability of the set point temperature to within ±0.2 °C were achieved by controlling the power input to the resistive heaters using Eurotherm 2408 temperature controllers. All experiments were conducted at a constant inert gas flow (controlled using a flow meter) to ensure reproducibility of temperature measurements. The temperature in the sample chamber of the HDAC was measured using NiCr-Ni thermocouples and calibrated before and after the experiments using the melting point of $NaNO_3$ at 1 atm pressure (306.8 °C) and the ice I+L+V triple point of water (0.01 °C, 0.6 kPa). No shift of the temperature calibration was detected. The accuracy of the temperature measurements was better than ±1 °C and the reproducibility was better than ±0.5 °C.

The sample used in this study (sample 062895-IX) was a disk of Brazilian quartz that contained synthetic pure water inclusions. The inclusions were formed by healing fractures in a quartz core at about 580 °C and 300 MPa following the

* E-mail: burnley@gsu.edu

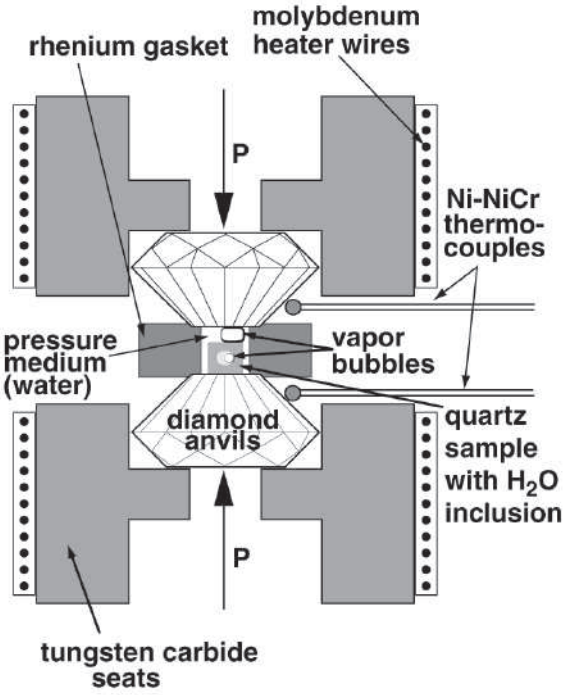

FIGURE 1. Schematic diagram of the experimental configuration. The sample chamber of the HDAC is located between the diamond anvils and had a diameter of sample chamber between 400 to 500 μm and a height of about 100 μm. A vapor bubble is trapped in the sample chamber along with water and the quartz sample, which contains the fluid inclusions.

procedure described by Bodnar and Sterner (1987). Disks of the quartz sample were created using a low-speed saw. The disks were polished on both sides to a thickness of 90 μm and their orientation with respect to the crystallographic axes of the quartz was determined optically. The **c** axis of the sample was nearly perpendicular to the polished faces of the disks. The inclusions studied were located midway between the polished faces and were roughly coplanar, i.e., the plane of the healed fracture was also approximately perpendicular to the **c** axis. A small conical disk with a diameter of about 300 μm was cut around the inclusions using a microscope-mounted cutter (U. Medenbach, Witten, Germany). The quartz disk with the selected inclusions was transferred into the sample chamber (in this study, a 500 μm hole in the Re gasket separating the anvils). First, the homogenization temperature of the inclusions was determined without sealing the sample chamber, i.e., the confining pressure was about 0.1 MPa. Then, chromatographic grade water was added as the pressure medium. Some of that liquid water was allowed to leak out, which produced an air bubble in the sample chamber before it was sealed by compression of the gasket between the anvils. Care was also taken that the upper diamond anvil did not come in contact with the quartz chip to ensure that the pressure on the sample was hydrostatic.

Upon heating the filled and sealed sample chamber, the *P-T* paths of the pressure medium and the inclusions were initially constrained by the liquid-vapor curve of water, because both consisted of liquid water (L) and a vapor bubble (V). In our experiments, the pressure medium had a higher L/V ratio and therefore a lower bulk molar volume than the inclusion. Therefore, the vapor bubble disappeared at a lower homogenization temperature to the liquid [Th(L + V → L)] and followed a steeper *P-T* path upon further heating. This resulted in an increasingly higher confining pressure on the sample, whereas the inclusions in the quartz disk were still at vapor pressure. This pressure difference caused a decrease in the inclusion volume, which translates into a lower molar volume, because no water is lost from the inclusion. After measurement of the homogenization temperature of the inclusions, the cell was cooled, and the homogenization temperature of the pressure medium was determined. During cooling, the change of the sample chamber volume is less than 0.5% (Bassett et al. 1993), which results in a close to isochoric decrease of the confining pressure. The sample was subjected to several heating cycles along different isochores by varying the L/V ratio in the sample chamber and thus the molar volume of the pressure medium at the start of each run. If no vapor was present in the pressure medium at any temperature, the ice I melting temperature was measured instead of Th(L + V → L). After the experiments, the homogenization temperature of the inclusion was determined again at 0.1 MPa confining pressure to check if the deformation of the quartz around the inclusions was completely elastic.

Because the phase diagram of water is well known and accurate equations of state are available, the molar volume of the inclusion and the pressure medium can be obtained from the homogenization temperatures and the pressure can be determined at any point given the temperature. The equation of state of H_2O of Haar et al. (1984) was used to calculate the molar volume and the homogenization pressure (i.e., the internal pressure) of the fluid inclusions from their homogenization temperature, and to obtain the confining pressure at Th(L + V → L) of the inclusion from the homogenization temperature of the pressure medium. Because this equation of state should not be applied at temperatures below 273.15 K, we used a different procedure for experiments in which no vapor bubble nucleated in the pressure medium upon cooling. In these cases, the pressure at the measured ice I liquidus temperature was calculated from the equation for the ice I melting curve provided by Wagner et al. (1994). The molar volume corresponding to that pressure and temperature and the confining pressure at the homogenization temperature of the inclusion were then obtained using the equation of state of H_2O of Saul and Wagner (1989). The error in the calculated pressure introduced by using two different equations of state is insignificant at the *P-T* conditions of our study, at most 1.37% at the maximum confining pressure [560.9 MPa from the EOS of Saul and Wagner (1989), vs. 553.3 MPa from the EOS of Haar et al. (1984) for the same molar volume and temperature]. The effect of quartz solubility on the volumetric properties of water and the inclusion volume is, likewise, negligible. For example, the solubility of quartz in water at the maximum homogenization temperature of our experiments (298 °C) is 0.0109 mol/kg (Rimstidt 1997). This corresponds to an increase in the molar volume of the inclusion of less than 0.005 cm^3/mol, which is not detectable by microthermometry.

The inclusion shape and dimensions were measured from optical photomicrographs of the sample. The shape can be fairly well characterized in two dimensions from photomicrographs. There is some uncertainty associated with the refraction of light around the edges of the inclusion and additional uncertainty introduced in creating a shape that can be meshed from the natural irregular shape of the inclusion; however these uncertainties are relatively small. In contrast, there are larger uncertainties in our knowledge of the profile of the inclusion in the third dimension. Inclusions I to V display a round outline in the plane parallel to the photograph (Fig. 2), i.e., they are of fairly low maturity (Roedder 1984). Thus, their cross section normal to the photograph should, likewise, not possess any sharp corners. The dimensions of the inclusions normal to the photograph were not determined because their thickness was close to or within the resolution of the optical microscope. However, their thickness can be constrained to 1 ± 0.5 μm based on the synthesis conditions. The inclusions were formed at about 580 °C and 300 MPa by healing fractures in a thermally shocked quartz core for 140 hours in water. TEM observations on inclusions synthesized at similar conditions (562 °C and 200 MPa) showed that elongated flat inclusions with a maximum length to width ratio of 10:1 formed within healed cracks of ≤1.5 μm thickness (Bakker and Jansen 1994). The thickness of inclusions in quartz synthesized by the fracture healing technique (Bodnar and Sterner 1987) varied between about 0.5 and 1.5 μm, as inferred from TEM micrographs after plastic deformation experiments (Schmidt et al. 2003; Vityk et al. 2000). The photograph of the inclusions (Fig. 2) shows that the dark rims at the liquid-vapor boundary caused by total reflection are quite narrow, which also points to a flat inclusion cross section.

Finite element modeling

We have used a commercially available engineering package, MSC. MARC/Mentat, to create and analyze two-dimensional (2D) and three-dimensional (3D) finite element models of the fluid inclusions studied experimentally. 2D models were constructed using 6-noded triangular elements (element 126 in the MARC library) that have a node at each vertex and at the midpoint of each side that allows a parabolic interpolation function to be used along each edge. These models were calculated assuming an axisymmetric or plane strain geometry utilizing full integration. Details of the procedure used to develop and

analyze 2D models, constitutive equations, and elastic constants are described in Burnley and Davis (2004).

All 3D model shapes have orthogonal symmetry. They were created using a combination of analytically generated toroidal, cylindrical, and rectangular solid surfaces The surfaces were added and subtracted to define an enclosed volume and deformed, creating $^1/_8$ of the desired shape. Each discrete surface of a model was individually meshed and then an automatic meshing routine was used to mesh the interior according to the mesh assigned to the exterior surfaces. The resulting model was constructed of four noded linear isoparametric tetrahedral elements. The finished $^1/_8$ model was then reflected through three orthogonal mirror planes and joined along the resulting inner surfaces. To reduce computational time, the overall size of the models was kept to a minimum. However, the outer surfaces of the models were far enough away from the inclusion to prevent flexure of the outer surfaces from making a contribution to the volume change. In the directions of the two larger dimensions of the inclusions, the outer boundary of the models was at a distance of at least four times the inclusion dimension. In the direction of the shortest dimension (which deforms the most), the outer boundary of the models was at a distance of at least 20 times the inclusion dimension.

The models were calculated as 3D solids assuming constant dilation using full integration. Since there is no central node on each element side, the element is integrated numerically at a single point at the centroid of the element and linear interpolation functions are used. The constitutive equation used by MARC for anisotropic linear elastic solids is:

$$\sigma_{ij} = \mathbf{C}_{ijkl}\varepsilon_{kl} \quad (1)$$

where σ_{ij} is the stress tensor, $\mathbf{C}_{ijkl}$ are the elastic stiffness moduli, and ε_{ij} is the strain tensor. For the 3D the models presented here, we use the single crystal elastic stiffness moduli listed in Table 1. The moduli were obtained by interpolation from the one atmosphere data for α-quartz of Ohno (1995), for the average homogenization temperature of the inclusions, which was 281 °C. The pressure and temperature dependence of the moduli are not included in these calculations. The data in our study was collected over a very limited range of temperature (273 to 298 °C). In this range, the effect of temperature on the C_{ij} is very small (Carpenter et al. 1998; Ohno 1995). The effect of neglecting the pressure dependence of the elastic moduli will be discussed below.

To facilitate calculation of the inclusion volume, the interior of the inclusion was meshed as well. Since the boundary conditions applied to the interior surface of the inclusion reproduce the response of the fluid, the material properties of the elements assigned to the inclusion must keep the inclusion from imposing any additional forces on the quartz. Therefore, the fluid elements were modeled as an isotropic linear elastic solid with a Young's modulus of 10^{-9} and Poisson's ratio of 0.5.

Boundary conditions

Pressure in the inclusion is modeled by the application of constant face loads that act perpendicular to the faces of elements on the internal boundary of the inclusion. To simulate the confining pressure, face loads were applied to elements on the external boundaries of the model. The distributed face loads are integrated using a single integration point at the centroid of the element face to which they are applied. Face loads in MARC are assumed to have the same units as the elastic moduli (e.g., GPa). To prevent rigid body rotation and translation, boundary conditions preventing translation in the x, y, or z directions were placed on three corners of the models. Although the face load boundary conditions and model shape have orthogonal symmetry they do not place any restriction on the deformation of the quartz, which is trigonal.

Results

Data from the HDAC experiments are presented in Table 2 and plotted in Figure 3. The molar volume of each of the inclusions is not exactly the same, which is probably due to small temperature fluctuations during synthesis. The range of homogenization temperatures of the six inclusions measured in the HDAC at 1 atm confining pressure is 295.6 to 297.5 °C (average 296.9 °C), which is within the scatter of the homogenization temperatures of other inclusions in sample 062895-IX (range 293.8 to 297.5 °C, average 295.2 °C, n = 24, obtained using a gas-flow heating/freezing stage). For an individual inclusion, the observed scatter in the obtained molar volumes at low external pressures is related to the attainable reproducibility of the homogenization temperature measurements of ±0.5 °C. Thus, the error in the determined molar volume changes is less than ±0.04 cm^3/mol (or about ±0.16%) at the conditions of our experiments. The inclusions are shown in Figure 2; their dimensions in the plane of the photograph are listed in Table 3. For inclusions V and VI the long dimension listed is the sum of a

Table 1. Single-crystal elastic stiffness moduli used for models (in GPa)

c_{11}	c_{22}	c_{33}	c_{44}	c_{55}	c_{66}
86.2	86.2	98.4	55.4	55.4	42.7
c_{12}	c_{13}	c_{14}	c_{23}	c_{24}	c_{56}
0.8	9.7	−18.9	9.7	18.9	18.9

Note: Moduli interpolated from data of (Ohno 1995) for α-quartz at 281 °C.

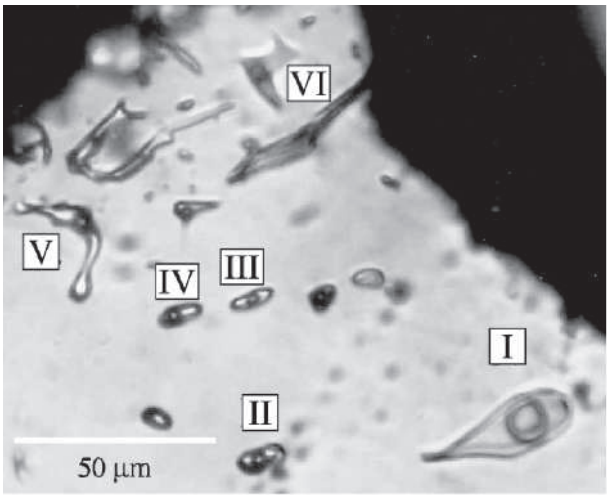

Figure 2. Photomicrograph of synthetic inclusions in quartz used in this study. The scale bar is 50 μm.

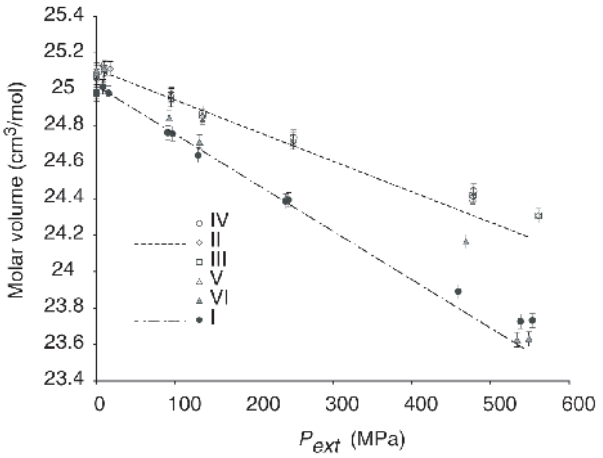

FIGURE 3. Plot of fluid inclusion molar volume vs. external confining pressure applied by the HDAC. Best fit lines for data between 0 and 250 MPa for inclusions I and II are plotted for reference.

series of line segments approximating the centerline within the inclusion. For inclusion I, the greater uncertainty in the long dimension originates from not knowing how much of the pinched off part of the inclusion should be considered. The dimensions of the inclusions normal to the photograph were not determined. However, as discussed above, we can safely assume that they are about 1 ± 0.5 µm thick.

To compare with results from the finite element models, the data from the synthetic fluid inclusions was recast in terms of percent volume change (%ΔV), which is equal to the percent change in molar volume, because the inclusions did not leak during the experiments. Therefore, $\%\Delta V = (V_{Pext} - V_{1atm})/V_{1atm} \times 100$, where V_{Pext} is the molar volume at a given external pressure and V_{1atm} is the molar volume at one atmosphere. To avoid any systematic uncertainty associated with potential differences in thermal gradients between the sample and the thermocouple when the HDAC was open vs. when it was closed and loaded, V_{1atm} for each inclusion was calculated using a second order polynomial fit of all data collected from that inclusion with the HDAC closed and pressurized. For the finite element models, $\%\Delta V = (V_{Pext} - V_{1atm})/V_{1atm} \times 100$, where V_{Pext} is the inclusion volume calculated at the same internal and external pressures as measured for the fluid inclusions and V_{1atm} is the volume of the inclusion calculated with an external pressure of 0.1 MPa and an internal pressure of 8.2 MPa. In general, %ΔV for linear elastic deformation of an inclusion can be depicted as a linear function of internal and external pressure (P_{ext}) (Burnley and Davis 2004). However, in this study the internal pressure variations are very small relative to the external pressure variations. Therefore, we compare the experimental data and model results by simply plotting %ΔV vs. P_{ext} as shown, for example, in Figure 4.

DISCUSSION

As is expected for linear elastic deformation, molar volume change for the synthetic inclusions, when loaded in the HDAC, fall along roughly linear trends as a function of external pressure (Fig. 3). The fact that the final and initial molar volumes are the same (see Table 2) also demonstrates that the deformation of

TABLE 2. Results from HDAC experiments

	Inclusions			Pressure medium	
Number	*Th*(L+V→L) (°C)	Molar volume (cm³/mol)	Internal Pressure (MPa)	*Th*(L+V→L) (°C) or *Tm*(Icel+L→L) (°C)	Confining Pressure (MPa) at *Th*(L+V→L) of inclusion
I	295.8	24.987	8.1	–*	0.1
	290.6	24.639	7.5	209.0	129.3
	295.7	24.980	8.1	288.2	15.6
	296.2	25.014	8.1	295.7	8.6
	296.2	25.014	8.1	305.0	8.1
	292.4	24.757	7.7	228.3	97.0
	292.5	24.763	7.7	232.1	90.6
	286.7	24.394	7.1	149.5	243.9
	286.6	24.387	7.1	151.1	240.3
	278.1	23.891	6.2	–0.4	459.2
	275.1	23.727	6.0	–3.6	538.0
	275.2	23.733	6.0	–4.3	553.2
	295.6	24.973	8.1	–*	0.1
II	296.8	25.056	8.2	–*	0.1
	293.8	24.850	7.9	209.0	134.4
	297.6	25.113	8.3	288.2	17.7
	297.2	25.084	8.2	295.7	9.7
	295.2	24.945	8.0	232.1	94.6
	291.7	24.711	7.6	151.1	249.5
	287.0	24.412	7.1	–0.4	477.5
	285.3	24.308	6.9	–3.6	560.9
	296.8	25.056	8.2	–*	0.1
III	297.0	25.070	8.2	–*	0.1
	294.0	24.864	7.9	209.0	134.7
	297.6	25.113	8.3	295.7	10.1
	295.5	24.966	8.1	232.1	95.0
	291.9	24.724	7.6	151.1	249.9
	287.1	24.418	7.1	–0.4	477.8
	285.3	24.308	6.9	–3.6	560.9
	297.1	25.077	8.2	–*	0.1
IV	297.0	25.070	8.2	–*	0.1
	294.1	24.870	7.9	209.0	134.9
	297.7	25.120	8.3	295.7	10.2
	295.6	24.973	8.1	232.1	95.1
	292.1	24.737	7.7	151.1	250.2
	287.5	24.443	7.2	–0.4	478.6
	297.1	25.077	8.2	–*	0.1
V	297.1	25.077	8.2	–*	0.1
	293.9	24.857	7.9	209.0	134.5
	298.0	25.141	8.3	305.0	8.3
	295.6	24.973	8.1	232.1	95.1
	291.6	24.704	7.6	151.1	249.3
	286.9	24.406	7.1	–0.4	477.3
	297.3	25.091	8.3	–*	0.1
VI	297.3	25.091	8.3	–*	0.1
	291.7	24.711	7.6	209.0	131.1
	297.6	25.113	8.3	295.7	10.1
	293.7	24.844	7.8	232.1	92.4
	286.9	24.406	7.1	151.1	240.8
	282.9	24.165	6.7	–0.4	469.1
	273.2	23.626	5.8	–3.6	533.8
	273.3	23.632	5.8	–4.3	548.9
	297.5	25.106	8.3	–*	0.1

Notes: Th(L + V→L) = liquid-vapor homogenization temperature, homogenization to the liquid phase; *Tm*(Icel + L → L) = ice I melting temperature in presence of liquid water (numbers below 0 °C).
* No pressure medium added, measurement at 0.1 MPa external pressure.

TABLE 3. Measured dimensions of inclusions

Inclusion	Narrow dimension (µm)	Long dimension (µm)
I	12(1)	30(6)
II	5(1)	11(1)
III	3.6(1.2)	10(1.5)
IV	4(1.2)	9.4(2)
V	4.6(2.5)	40(2)
VI	4(1)	20.4(1)

Note: Uncertainty listed in parenthesis.

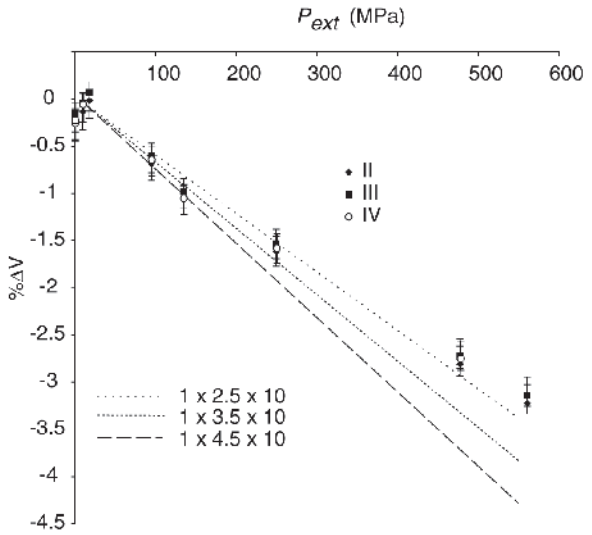

FIGURE 4. Plot comparing percent volume change of synthetic inclusions II, III, and IV with calculated volume changes from finite element models with dimensions $1 \times 2.5 \times 10$, $1 \times 3.5 \times 10$, and $1 \times 4.5 \times 10$. The shape of the models is shown in Figure 6a.

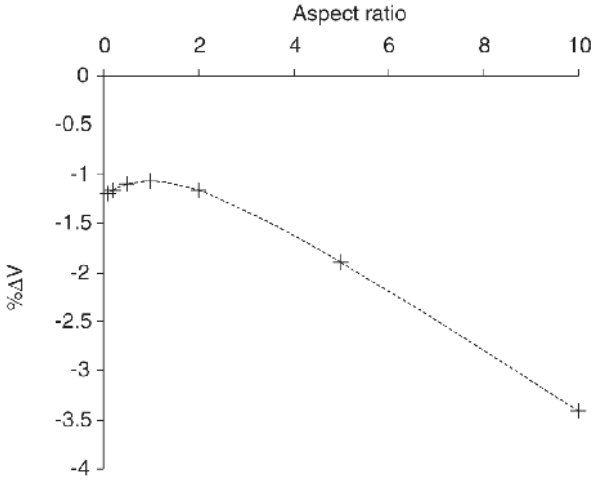

FIGURE 5. Percent volume change experienced by axisymmetric ellipsoids in "isotropic" quartz at 7.62 MPa internal pressure and 248.5 MPa external pressure plotted vs. aspect ratio (where the rotational axis of the ellipsoid is the denominator). Prolate ellipsoids plot with aspect ratios less than one and oblate ellipsoids plot as greater than 1.

the inclusions at high external pressure was elastic and that the inclusions did not leak. As pressure increases the deviation from linearity becomes more apparent because the elastic moduli of quartz are pressure dependent (McSkimin et al. 1965). Since the finite element models utilize only linear elastic behavior, we only used the data at and below 250 MPa to judge how well a finite element model fits data from the synthetic inclusions. The purpose of this study is to see if finite element models that reasonably approximate the shapes of the inclusions can reproduce the elastic volume changes observed when the inclusions experience differential pressure. Burnley and Davis (2004) have shown that the shape of an inclusion should strongly affect the elastic volume change experienced under a given set of conditions. However, a particular volume change behavior is not unique. In other words, two inclusions with completely different shapes may have the same volume change behavior. This is illustrated in Figure 5, which shows results from 2D axisymmetric models in "isotropic" quartz that were published in Burnley and Davis (2004). In Figure 5, the volume change experienced by axisymmetric ellipsoids at 7.62 MPa internal pressure and 248.5 MPa external pressure is plotted vs. the aspect ratio of the ellipse. Prolate ellipsoids plot with aspect ratios less than one and oblate ellipsoids plot as greater than one. A volume change between –1.07% and –1.9% can be produced by either a prolate or oblate ellipsoid. It is also clear from Figure 5 that any observed volume change above –1.07% can be produced by an oblate ellipsoid by choosing the appropriate aspect ratio. Therefore, showing that a finite element model can match the exact volume change behavior of an inclusion is not particularly meaningful. What is meaningful is to demonstrate that a model that closely approximates the shape and crystallographic orientation of an inclusion also reproduces the volume change behavior.

Inclusions II, III, and IV exhibit very similar volume change behavior and have very similar shapes in the plane of the photograph. Their volume changes are fit well by a flat-sided model inclusion with dimensions $1 \times 3.5 \times 10$ oriented with the short dimension parallel to the **c** axis of the host quartz (Fig. 4). The shape of this inclusion was constructed by joining a 1×3 cylinder to a torus with a radius of 1 and deforming the resulting shape so that it has dimensions $1 \times 3.5 \times 10$ (Fig. 6a). Volume changes for flat-sided model inclusion with dimensions $1 \times 2.5 \times 10$ and $1 \times 4.5 \times 10$ are also shown in Figure 4. The dimensions for these inclusions are within the boundaries of what can be considered reasonable matches to the real inclusions, but they do not match the volume change data as well. As discussed above, by adjusting the dimensions of a model inclusion the match between the experimental data from the inclusion and the models can be made arbitrarily good for many inclusion shapes. However the dimensions of the resulting shape may not match those of the actual inclusion. For example we found that matching the volume change of inclusions II, III, and IV with a flat-sided model inclusion with angular terminations (constructed from truncated cones) or with a smooth elliptical inclusion (constructed by deforming a sphere) resulted in inclusions that were either too thick or too narrow to reasonably match the real inclusions.

The volume change as a function of pressure for inclusion V is very similar to that exhibited by inclusions II, III, and IV (Fig. 3). This may seem surprising because the shape of inclusion V differs significantly from that of II, III, and IV; it has a much higher aspect ratio and it is curved into a "u" shape. However, there are several reasons why this is not an unexpected result. Analytical calculations of the compressibility of ellipsoidal pores in bulk quartz show that the compressibility of an axisymmetric prolate ellipsoid (cigar shaped) becomes less sensitive to the length of the ellipsoid as its length increases (Zimmerman 1991). This effect can also be observed in Figure 5. This makes intuitive sense because, as the ends of the inclusion get further and further away, the volume change becomes dominated by the behavior of the cross sectional area normal to the long axis

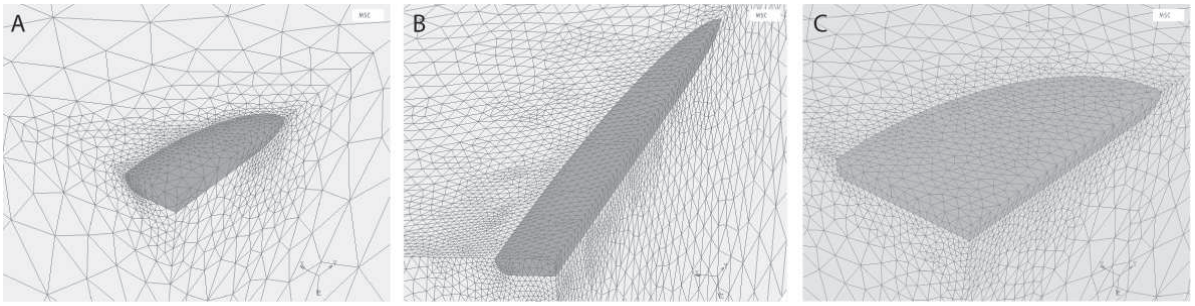

FIGURE 6. 3D Finite element model meshes for inclusions with dimensions (**a**) $1 \times 3.5 \times 10$, (**b**) $1 \times 3.5 \times 40$, and (**c**) $1.5 \times 12 \times 24$. The shaded region is the inclusion. Only an eighth of each model is shown. The remainder of each model is related to the part shown by reflection through three orthogonal mirror planes, as described in the text.

of the ellipsoid. Inclusions II, III, IV, and V are not axisymmetric prolate ellipsoids but a similar reasoning can apply; as one dimension becomes significantly larger than the others, the behavior of the cross sectional area normal to that dimension has more and more influence on the volume change. Thus, as can been seen in Figure 7, stretching the long axis of the flat sided inclusions used above from $1 \times 3.5 \times 10$ to $1 \times 3.5 \times 40$ (Fig. 6b) does not make a large difference in the volume change behavior. The longer inclusion is slightly more compliant as is inclusion V relative to inclusions II, III, and IV. Again, the **c** axis of the quartz host is oriented parallel to the shortest dimension. Another difference among inclusions II, III, IV, and V is that inclusion V is curved (in the (001) plane). For the curvature to impact the volume change of any given unit length of the inclusion, stresses from other parts of the inclusion would have to reach the quartz host immediately adjacent to the inclusion. To test this effect, we constructed plane strain models of two channels at varying distances from each other. To maximize the effect, we choose to model flat channels with a pointed profile, which creates a larger stress concentration than an inclusion with a smooth profile. The change in cross sectional area as a function of distance between the channels is plotted in Figure 8, where the inset shows one of the models. To "feel" each other, the two channels need be within a distance comparable to their width. Inclusion V is not that tightly curved, so using a straight model is justified.

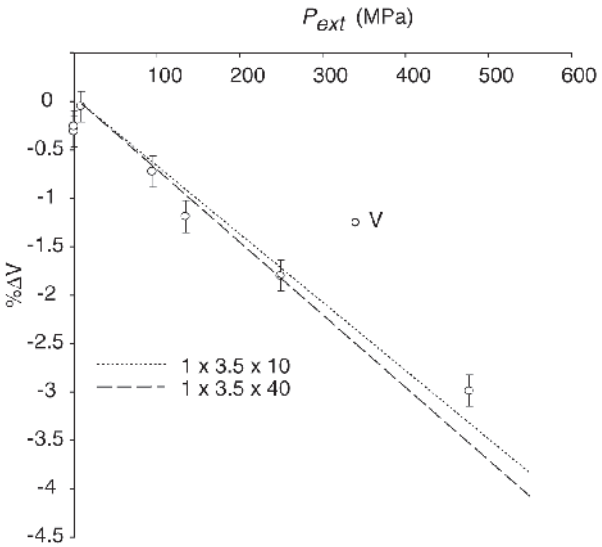

FIGURE 7. Plot comparing percent volume change of synthetic inclusion V with calculated volume changes from finite element models with dimensions of $1 \times 3.5 \times 10$ and $1 \times 3.5 \times 40$. The shape of the model inclusions is shown in Figures 6a and 6b. Note that increasing the length of the longest axis by a factor of four has relatively little impact on the volume change.

Inclusion I is significantly larger than the other inclusions and it experiences significantly more volume change than the other inclusions. The shape of inclusion I deviates from an ellipsoid in plan view because it pinches off at one end. However, with the exception of the pinched end, the inclusion is generally elliptical in shape; the largest ellipse that can be inscribed within the outline of inclusion I measures 12×24 μm. The volume change for this inclusion can be matched by an inclusion constructed by joining a 1.5×11 cylinder to a toroid with a radius of 1 and deforming the resulting shape so that it has dimensions $1.5 \times 12 \times 24$ (Fig. 6c). A model inclusion with dimensions $1 \times 12 \times 24$ gives much larger volume changes than are observed for inclusion I. The percent volume change is very sensitive to the thickness of the model inclusion. This is illustrated in Figure 9 where the effect of changing the thickness of the inclusion from 1.3 to 1.7 is shown. That the thickness of the inclusion would have a strong effect on the percent volume change of a pancake shape inclusion makes intuitive sense. Most of the volume change comes from deformation of the large flat surface of the inclusion. This deformation will be little affected by the height of the edge of the inclusion. Therefore the thinner the inclusion, the greater the relative volume change will be. As discussed earlier, the thickness of the inclusions used in this study can only be constrained to 1 ± 0.5 μm. The models suggest that inclusion I is slightly thicker than the other inclusions, which is entirely possible. This sensitivity of the volume change to the inclusion aspect ratio could be exploited as a nondestructive way to determine the thickness of flat "secondary" inclusions, which is generally smaller than can be resolved with optical microscopy.

Inclusion VI was not modeled due to its irregular shape. In particular, the thickness of the inclusion does not appear to be constant from one end to the other as judged by the refraction of light along its edge. The width and total length of the inclusion are in a similar range as those of inclusions II–V, so at first glance, one would expect its volume change behavior to be similar. However, inclusion VI is more compliant than the

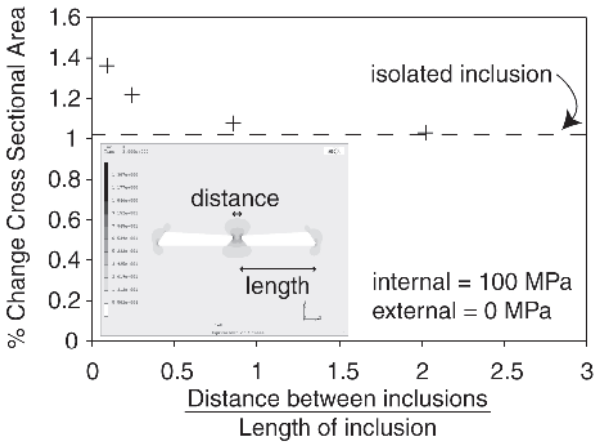

FIGURE 8. Change in cross sectional area as a function of distance between two pressurized channels calculated using 2D plane strain models. The distance between the channels is normalized by the width of the channel. The inset shows the distribution of differential stress in GPa around the inclusion channels for the case where the distance between inclusions/length of inclusion = 0.09.

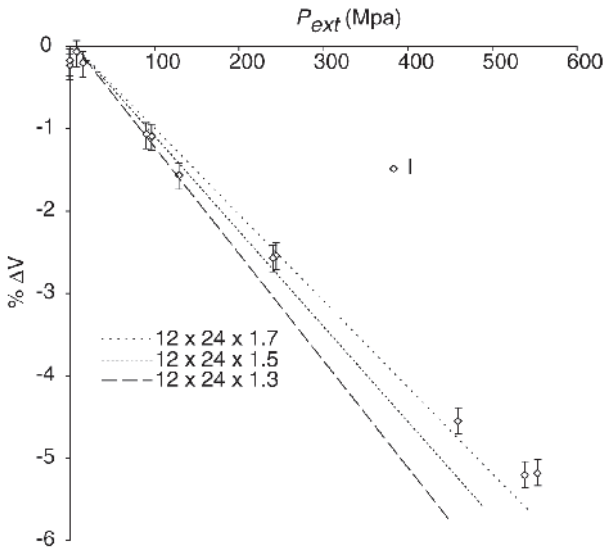

FIGURE 9. Plot comparing percent volume change of synthetic inclusion I with calculated volume changes from finite element models with dimensions of $1.3 \times 12 \times 24$, $1.5 \times 12 \times 24$, and $1.7 \times 12 \times 24$. The shape of the models is shown in Figure 6c. Percent volume change of the model is strongly sensitive to the thickness of the model.

other inclusions. This is consistent with all or part of inclusion VI being thinner.

In summary, we are able to match the volume changes of synthetic fluid inclusions experiencing changes in external pressure, with finite element models that reasonably approximate the shapes of the inclusion for external pressures under 250 MPa. For large pressure excursions, an elastic model that incorporates the pressure derivatives of the elastic moduli is required.

This study gives us confidence that finite element models may be used to predict the elastic behavior of inclusions in situations where confirmation of model results is not possible. For example, Sobolev et al. (2000) recently demonstrated that micro-Raman spectroscopy and microcrystal X-ray diffraction can be used to measure the pressures inside coesite inclusions trapped in diamond. Since they observed no evidence for ductile deformation or brittle failure of the diamond host, they argued that they could calculate the original trapping pressure for the inclusion using the theoretical equation for a pressurized spherical hole in an elastic medium. Our results demonstrate that taking the inclusion shape into account measurably improves our ability to match model elastic volume changes to observed volume changes of inclusions. Therefore, it follows directly that finite element models based on the actual shape of coesite inclusions (which were described as triangular) should improve estimates of mantle trapping pressures derived from such a coesite in diamond geobarometer.

In addition to volumetric information, the finite element models contain detailed information about the stress distribution in the host (e.g., Fig. 8 inset). There are several situations where a quantitative understanding of the pattern and levels of stresses in the host around an inclusion could lead to new scientific understanding. For example, solid inclusions in minerals recovered from depth are often surrounded by patterns of cracks in the host (e.g., Whitney et al. 2000). Combined with experimental data on fracture toughness, FEM could be used to estimate the pressure differential required to produce the fractures and therefore set bounds on the uplift path of the host rock. FEM could also be used in conjunction with experimental deformation studies. Schmidt et al. (2003) observed a minimum in the creep strength of quartz associated with the α-β transformation by studying the pressure differential required to induce permanent volume changes in fluid inclusions. Finite element models of the inclusions could be used to estimate the flow stress of the inclusion host. Although demonstrating that we can match the elastic volume change of an inclusion does not demonstrate that the pattern of stresses that produce the elastic volume change are modeled correctly, it is an important check of the model results that gives us confidence to proceed with further modeling studies.

ACKNOWLEDGMENTS

This work was supported by National Science Foundation grant EAR-0136107. Burnley thanks Yunghui Hu for assistance with model mesh generation. The authors thank David Bruhn for the initial inspiration for doing this project and for helpful conversations, and Matthias Gottschalk for providing computer programs for different equations of state. The authors also thank Bill Bassett and two anonymous reviewers for insightful comments and suggestions.

REFERENCE CITED

Bakker, R.J. and Jansen, J.B. (1994) A mechanism for preferential H_2O leakage from the fluid inclusions in quartz, based on TEM observations. Contributions to Mineralogy and Petrology, 116, 7–20.

Bassett, W.A., Shen, A.H., Bucknam, M., and Chou, I.-M. (1993) A new diamond anvil cell for hydrothermal studies to 2.5 GPa and from –190 to 1200 C. Reviews of Scientific Instruments, 64, 2340–2345.

Bodnar, R.J. and Sterner, S.M. (1987) Synthetic Fluid Inclusions. In G.C. Ulmer and H.L. Barnes, Eds., Hydrothermal Experimental Techniques, p. 423-457. Wiley, New York.

Burnley, P.C. and Davis, M.K. (2004) Volume Changes in Fluid Inclusions Produced by Heating and Pressurization: An Assessment by Finite Element Modeling. Canadian Mineralogist, 42, 1369–1382.

Carpenter, M.A., Salje, E.K.H., Graeme-Barber, A., Wruck, B., Dove, M.T. and Knight, K.S. (1998) Calibration of excess thermodynamic properties and elastic constant variations associated with the $\alpha \leftrightarrow \beta$ phase transition in quartz. American Mineralogist, 83, 2–22.

Darling, R.S. and Bassett, W.A. (2002) Analysis of natural H_2O + CO_2 + NaCl fluid inclusions in the hydrothermal diamond anvil cell. American Mineralogist, 87, 69–78.

Haar, L., Gallagher, J.S., and Kell, G.S. (1984) NBS/NRC Steam Tables: Thermodynamic and transport properties and computer programs for vapor and liquid states of water in SI units. Hemisphere Publishing Company, Washington, D.C.

Kenkmann, T. and Dresen, G. (1998) Stress gradients around porphyroclasts: palaeopiezometric estimates and numerical modeling. Journal of Structural Geology, 20, 163–173.

McSkimin, H.J., Andreatch, P., and Thurston, R.N. (1965) Elastic Moduli of quartz versus hydrostatic pressure at 25° and –195.8°. Journal of Applied Physics, 36, 1625–1632.

Ohno, I. (1995) Temperature variation of elastic properties of α-quartz up to the α–β transition. Journal of Physics of the Earth, 43, 157–169.

Rimstidt, J.D. (1997) Quartz solubility at low temperatures. Geochimica et Cosmochimica Acta, 61, 2553–2558.

Roedder, E. (1984) Fluid Inclusions. 644 p. Mineral Society of America, Washington, D.C.

Saul, A. and Wagner, W. (1989) A fundamental equation for water covering the range from the melting line to 1273 K at pressures 25,000 MPa. Journal of Physics and Chemical Reference Data, 18, 1537–1564.

Schmidt, C., Chou, I.M., Bodnar, R.D., and Bassett, W.A. (1998) Microthermometric analysis of synthetic fluid inclusions in the hydrothermal diamond-anvil cell. American Mineralogist, 83, 995–1007.

Schmidt, C., Bruhn, D., and Wirth, R. (2003) Experimental evidence of transformation plasticity in silicates: Minimum of creep strength in quartz. Earth and Planetary Science Letters, 205, 273–280.

Sobolev, N.V., Fursenko, B. A., Goryainov, S.V., Shu, J., Hemley, R.J., Mao, H-K., and Boyd, F.R. (2000) Fossilized high pressure from the Earth's deep interior: The coesite-in-diamond barometer. Proceedings of the National Academy of Sciences, 97, 11875–11879.

Vityk, M.O., Bodnar, R.J., and Doukhan, J.-C. (2000) Synthetic fluid inclusions. XV. TEM investigation of plastic flow associated with reequilibration of fluid inclusions in natural quartz. Contributions to Mineralogy and Petrology, 139, 285–297.

Wagner, W., Saul, A., and Pruss, A. (1994) International equations for the pressure along the melting and along the sublimation curve of ordinary water substance. Journal of Physics and Chemical Reference Data, 23, 515–527.

Whitney, D.L., Cooke, M.L., and Du Frane, S.A. (2000) Modeling of radial microcracks at corners of inclusions in garnet using fracture mechanics. Journal of Geophysical Research, Solid Earth, 105, 2843–2853.

Zimmerman, R.W. (1991) Compressibility of Sandstone. Developments in Petroleum Sciences, p. 173. Elsevier, Amsterdam.

MANUSCRIPT RECEIVED JULY 14, 2005
MANUSCRIPT ACCEPTED JUNE 15, 2006
MANUSCRIPT HANDLED BY PRZEMYSLAW DERA